Determining Brown's Characteristic Curves using Molecular Simulation

Maximilian Urschel and Simon Stephan*

Laboratory of Engineering Thermodynamics (LTD), TU Kaiserslautern, Kaiserslautern, 67663, Germany

E-mail: Simon.Stephan@rptu.de

Abstract

Brown's characteristic curves define lines on the thermodynamic surface where special thermodynamic conditions hold. These curves are an important tool for the development of thermodynamic models of fluids. Yet, practically no experimental data for Brown's characteristic curves is available. In this work, a rigorous and generalized method for determining Brown's characteristic curves based on molecular simulation was developed. As multiple thermodynamic equivalent definitions apply for the characteristic curves, different simulation routes were compared. Based on this systematic approach, the most favorable route for determining each characteristic curve was identified. The computational procedure developed in this work combines molecular simulation, molecular-based equation of state, and the evaluation of the second virial coefficient. The new method was tested on a simple model system (the classical Lennard-Jones fluid) and different types of real substances (toluene, methane, ethane, propane, and ethanol). It is thereby shown that the method is robust and yields accurate results. Moreover, a computer code implementation of the method is presented.

Introduction

Brown's characteristic curves define lines on the thermodynamic equilibrium surface. Each of the characteristic curves has – for a given thermophysical property – the same behavior as the ideal gas.[1] The four characteristic curves are the Zeno, Amagat, Boyle, and Charles curve. These curves are located within a large pressure and temperature range. For a molecular fluid, Brown's characteristic curves are known to exhibit certain thermodynamic features.[1] Therefore, Brown's characteristic curves have become an important tool for the assessment of the extrapolation behavior of new equations of state (EOS).[2–4] This test has also been included in the IUPAC guidelines for publishing new EOS.[5] Nevertheless, due to the extreme conditions, there is practically no experimental data available on the characteristic curves. Molecular simulation based on force fields provides an attractive alternative to classical laboratory experiments, which is explored in this work. The four characteristic curves are also known by other names. The Zeno curve is at times simply called *ideal curve*. The Amagat curve is also called *Joule inversion curve*, and the Charles curve is often called *Joule-Thomson inversion curve*. In this work, the original names introduced by Brown[1] are used.

Brown's characteristic curves are usually discussed in the double logarithmic pressure-temperature projection as schematically shown in Fig. 1. In this representation, all four characteristic curves exhibit a concave dome shape. Thereby, each characteristic curve exhibits a single pressure maximum. Moreover, Brown postulated three specific points where the characteristic curves contact each other:[1] the Zeno and Charles curve intersect each other in the pressure maximum of the Zeno curve, the Zeno and Boyle curve converge into each other in their zero-density limit $\rho \to 0$ at the Boyle temperature (zero-crossing point of second virial coefficient), and the Zeno and Amagat curve intersect each other at low temperatures. The Zeno and Amagat curve are usually truncated by the solid-liquid equilibrium at low temperatures. The Amagat, Boyle, and Charles curve must not have an intersection point. Instead, the Amagat curve surrounds the Charles curve and the Charles curve surrounds

the Boyle curve in the p-T projection, cf. Fig. 1. The Boyle and Charles curve originate on the vapor pressure curve. More specifically, the Charles curve originates on the binodal and the Boyle curve on the liquid-side spinodal. Moreover, all four characteristic curves circulate around the critical point in the p-T projection – even though the Boyle curve passes the critical point in close proximity, cf. Fig. 1. Furthermore, the temperature of the zero-density limit $\rho \to 0$ of the characteristic curves is directly linked to specific points of the second virial coefficient, cf. Fig. 1.

Brown deduced based on rational thermodynamics that one 0^{th}-order and three 1^{st}-order characteristic curves exist for a simple molecular fluid. For state points on the 0^{th}-order curve, the compressibility factor Z is unity, i.e.

$$Z = \frac{pv}{TR} = 1 \ , \tag{1}$$

where R indicates the universal gas constant and the specific volume is $v = 1/\rho$. The 0^{th}-order characteristic curve is called Zeno curve.

For state points on the three 1^{st}-order characteristic curves, the temperature, pressure, and density derivative of the compressibility factor, respectively, correspond to the ideal gas values, i.e. are zero.[1] For the Amagat curve, the temperature derivative of Z at isochoric conditions is zero

$$\left(\frac{\partial Z}{\partial T}\right)_v = 0 \ . \tag{2}$$

For the Boyle curve, the pressure derivative of Z at isothermal conditions is zero

$$\left(\frac{\partial Z}{\partial p}\right)_T = 0 \ . \tag{3}$$

For the Charles curve, the specific volume derivative of Z at isobaric conditions is zero

$$\left(\frac{\partial Z}{\partial v}\right)_p = 0 \ . \tag{4}$$

Several thermodynamic equivalent conditions formulated in other variables can be derived from the conditions (1)-(4).[3,6] Table 1 gives an overview of the most relevant conditions based on the molar enthalpy $h = H/N$, the molar internal energy $u = U/N$, and molar Helmholtz energy $a = A/N$. For the Helmholtz energy derivatives, the following short-hand notation is used

$$\tilde{a}_{kl} = (1/T)^k \rho^l \frac{\partial^{k+l} \tilde{a}}{\partial (1/T)^k \partial \rho^l} \ , \tag{5}$$

where $\tilde{a} = a/(k_\mathrm{B}T)$ indicates the reduced Helmholtz energy with k_B being the Boltzmann constant.

For the evaluation of the characteristic curves from an algebraic thermodynamic model, e.g. an EOS, the different conditions (cf. Table 1) are practically equivalent. This does however not hold for molecular simulations, which are computationally and numerically more demanding. For evaluating the different thermodynamic conditions (cf. Table 1) from a molecular simulation, different algorithms and simulation methods have to be applied for the sampling that go hand in hand with different statistical and systematic uncertainties as well as required computer time. There is presently no information available on the advantages and disadvantages of the different thermodynamic sampling routes for determining characteristic curve state points, cf. Table 1.

The Charles curve, a.k.a. Joule-Thomson inversion curve, has been at times studied using molecular simulations.[7–13] Molecular simulation data for all four characteristic curves has been reported only rarely and only for simple models.[6,14] In most cases, no statistical uncertainties were reported. In this work, we developed a generalized approach for determining Brown's characteristic curves of a given force field of a molecular fluid. We demonstrate the general applicability of the computational procedure by determining Brown's characteristic curves for different types of substances (model fluid, alkane, alcohol, and aromatic component). The new approach combines molecular-based equation of state calculations for determining initial guess values for the characteristic curves and three sequential molecular simulation steps. In the first simulation step, the second virial coefficient is determined,

which provides the zero-density limit state points of the characteristic curves. In the second simulation step, simulations are systematically carried out in the vicinity of the initial guess values, which provides the characteristic curve state points of the given force field. In the third simulation step, an additional simulation is carried out at each determined characteristic curve state point. For the second simulation step, different thermodynamic conditions (cf. Table 1) were systematically compared in this work. Thereby, the most favorable route was identified for each characteristic curve.

The rigorous approach proposed in this work has several advantages: (a) it can be applied to both simple model fluids and complex molecular fluids; (b) statistical uncertainties of the characteristic curve state points are estimated; (c) the thermodynamic consistency of the results is assessed by the method itself; (d) characteristic curve state points are also obtained for the vapor-liquid and solid-liquid metastable regions; (e) high-accurate results for the characteristic curves are appended in the zero-density limit (obtained from the virial route).

For applying the computational procedure, we provide a source code implementation of the entire simulation workflow that can be straightforwardly used in combination with a given simulation engine. In this work, the simulation engine *ms*2[15] was used in combination with the MolMod database.[16]

The method was applied to six substances to demonstrate its general applicability: the classical Lennard-Jones (LJ) model fluid[14] (used for validation with results from the literature); toluene, methane (using the Lennard-Jones fluid results), ethane, propane, and ethanol as real substance fluids; and the Lennard-Jones truncated and shifted (LJTS) fluid, which is an important model fluid in computational physics and physical chemistry.[17–23]

This work is structured as follows: first, the method and tools are introduced. Then, results for the fluids are presented and discussed (in parts in the Supporting Information). All primary simulation data is reported in the electronic Supporting Information.

Development of Computational Procedure

In the following, the method for determining Brown's characteristic curves using molecular simulation is presented. This section is structured as follows: first, an overview of the computational procedure is given. Then, the central elements are discussed in more detail following the sequential order of the algorithm, i.e. the determination of the initial guess values, the setting-up of the simulation points, details on the molecular simulations, and the evaluation of the characteristic curve state points and their statistical uncertainties as well as the assessment of their thermodynamic consistency. Moreover, the Matlab implementation of the algorithm is presented.

Overview

Fig. 2 gives an overview of the method. It can be applied to an arbitrary molecular fluid described by a force field. At the core of the method, molecular simulations are carried out in three steps that are mediated by molecular-based equation of state calculations. The algorithm is structured in four parts.

First, initial guess values for all three characteristic curves are calculated using a molecular-based EOS in combination with second virial coefficient data (purple part in Fig. 2). The latter is directly obtained from the force field. Thus, all four characteristic curves as well as the vapor-liquid equilibrium are computed from the EOS. Using the virial coefficient data of the force field, the zero-density limit of the EOS characteristic curve data is corrected such that the limit of the initial guess values converge to the correct limit. The second virial coefficient is computed from Mayer's f-function by averaging over numerous random orientations at different radii based on a Monte Carlo approach.[24] Alternatively, for simple (e.g. spherical) force fields, the integration of Mayer's f-function can be carried out directly by integration of the interaction potential. Both routes yield high accurate virial coefficient data and are part of the implementation of the algorithm (see below).

Second, based on the virial coefficient-corrected EOS initial guess values, homogeneous state molecular simulations are carried out (green part in Fig. 2). Therefore, a simulation state point set is generated as a grid in the vicinity of the initial guess values for each characteristic curve. For the evaluation of the different thermodynamic conditions (cf. Table 1), different state point grids are required. A state point grid consists of multiple sets of simulation points; each set of simulation points is used to determine one state point on a given characteristic curve. Depending on the thermodynamic condition, the state points within a set of simulation points are defined at a constant thermodynamic variable X, e.g. the temperature (see details below). Depending on the considered fluid, the used force field, and the reliability of the initial guess values, the width of the simulation state point grid should be adapted. For each state point on the grid characterized by a second thermodynamic variable Y, a molecular simulation is carried out to sample the values required for the evaluation of the applied condition of a thermodynamic property W, e.g. the compressibility factor (cf. Table 1). For determining a characteristic curve state point, each simulation set is evaluated independently. The respective thermodynamic condition is applied by fitting a second-order polynomial function to the results from each simulation set. The polynomial function is evaluated such that the thermodynamic variable Y, e.g. the density, specifying the characteristic curve state point is determined. As a simulation set is specified with one thermodynamic variable X being constant (and known), the characteristic curve state point is known at this point by two independent variables X, Y (two out of pvT).

Third, the statistical uncertainties of the characteristic curve state points are estimated from the statistical uncertainties of the simulation results of each individual state point of a given set using error propagation (red part in Fig. 2).

Finally (blue part in Fig. 2), an additional simulation is carried out for each characteristic curve state point to obtain further thermodynamic properties and in particular the state variable Z (third out of pvT). The state points obtained for the four characteristic curves from the molecular simulation sets are moreover extended by the zero-density limit charac-

teristic curve state points obtained from the virial route. Based on all compiled results, the thermodynamic consistency of the results is assessed.

In this work, different thermodynamic conditions (cf. Table 1) and different types of simulation state point grids (cf. Fig. 3) were used and compared regarding their computational efficiency, robustness, and accuracy. Here, the simulations were carried out in the NVT or NpT ensemble (but also other ensembles could in general be used).

The method outlined here is in general compatible with any molecular simulation engine. Also, both MD and MC sampling can in general be applied. In this work, the simulation code *ms*2 was used[15,24,25] for testing the method. The code *ms*2 can be used beneficially in the computational procedure proposed in this work as it automatically samples a large number of thermodynamic properties, including the Helmholtz energy derivatives with respect to density and inverse temperature using the *Lustig* formalism.[26–28] Thereby, a large number of thermodynamic characteristic curve conditions can be tested and consistency tests be applied.

The computational procedure proposed in this work was tested on different types of substances. For determining the most favorable sampling method, the Lennard-Jones fluid and toluene were used. Then, the most favorable sampling route was moreover tested on ethane, propane, ethanol, and the LJTS fluid. For all substances, rigid united atom force fields were used, i.e. no internal degrees of freedom were considered and hydrogen atoms in CH, CH_2, and CH_3 groups were implicitly modeled as fused interaction sites. For toluene, the force field proposed by *Guevara-Carrion et al.*[29] was used, which consists of seven Lennard-Jones interactions sites – each modeling a CH_x group – and six point quadrupole moments that model the π-orbital of the aromatic component. For ethane, the force field of *Vrabec et al*[30] was used, which consists of two Lennard-Jones interaction sites modeling the two methyl groups. For propane, the rigid version of the force field proposed by *Martin and Siepmann*[31] was used. It consists of three Lennard-Jones interactions sites modeling the methylene group and the two methyl groups. For ethanol, the force field proposed by *Schnabel et al*[32] was

used, which consists of three Lennard-Jones interaction sites modeling the the methylene and methyl group as well as the oxygen atom. It moreover consists of three point charges modeling the polarity of the molecule – in particular for capturing the ability for hydrogen bonding. For methane, the model proposed by *Vrabec et al.*[33] was used, which consists of a single Lennard-Jones interaction site. Therefore, the Lennard-Jones fluid simulation results were used for modeling methane by applying the reduced units principle.

Initial Guess Values and Setup of Simulations

Molecular-Based Equation of State

A molecular-based EOS is used for computing initial guess values for the four characteristic curves as well as the VLE. For molecular-based EOS, the component-specific parameters are usually fitted to VLE data, i.e. saturated densities and the vapor pressure. Due to the strong physical backbone of molecular-based EOS, these models often allow an extrapolation to extreme conditions.[3,34] Examples are the SPHCT EOS[35] and the SAFT-VR Mie EOS.[36] Equations of state used within the computational procedure proposed in this work are required to produce physically correct characteristic curves, which is not the case for all EOS.[3,37] Moreover, the EOS should have a physically realistic behavior in the VLE two-phase region as the Boyle curve originates on the spinodal. Hence, the EOS has to be carefully selected. Moreover, depending on the accuracy of the EOS, the width of the stimulation state point grid has to be adapted.

Here, the SAFT-VR Mie EOS[36] was used for demonstration purposes. The pure component parameters used in this work for modeling methane, ethane, propane, ethanol, and toluene are reported in the Supporting Information. For ethane, propane, and toluene, the chain term was used. For ethanol, additionally, the SAFT association term[38] was used. In the case that no pure component parameters for a reliable molecular-based EOS are available to determine initial guess values, such can simply be obtained using the corresponding states principle. Hence, using EOS results for the characteristic curves for a simple fluid, e.g.

the Lennard-Jones fluid,[3] and scaling those with the critical parameters of the studied fluid. This approach is demonstrated here (see Supporting Information) for the Lennard-Jones truncated and shifted (LJTS) fluid, where no EOS is presently available that extrapolates well to high pressure. Nevertheless, upon applying this corresponding states principle route, the simulation state point grid should be adapted.

Characteristic Curve Zero-Density Limit from Second Virial Coefficient

The characteristic curve initial guess values at low densities are sensitive for the computational procedure. If the zero-density limit obtained from the EOS deviates significantly from the corresponding force field values, the simulations at low densities become erroneous. Therefore, the force field second virial coefficient is taken into account already for the initial guess values. This is done by scaling the EOS results in the vicinity of the zero-density limit. Thereby, the corrected initial guess values converge to force field characteristic curve results at $\rho \to 0$.

The scaling is applied for all four characteristic curves using the corresponding characteristic second virial coefficient values, cf. Fig. 1. Therefore, the second virial coefficient is determined in a wide temperature range by sampling Mayer's f-function from the intermolecular interactions at different configurations as[39,40]

$$B = -2\pi \int_0^\infty \left\langle \exp\left(-\frac{u_{ij}(r_{ij}, \boldsymbol{\omega}_i, \boldsymbol{\omega}_j)}{k_\mathrm{B}T}\right) - 1 \right\rangle_{\boldsymbol{\omega}_i, \boldsymbol{\omega}_j} r_{ij}^2 \, \mathrm{d}r \ , \tag{6}$$

where u_{ij} indicates the intermolecular potential, r_{ij} indicates the center of mass distance between two molecules i and j, and the $\langle ... \rangle$ brackets indicate the averaging over different orientation $\boldsymbol{\omega}_i$ and $\boldsymbol{\omega}_j$. Monte Carlo molecular simulations are carried out for evaluating Eq. (6) at a given temperature. Thereby, randomly generated distances and orientations are evaluated. For large flexible molecules (not considered in this work), also different conformations are to be considered.

For simple spherical model potentials, Eq. (6) simplifies to

$$B = -2\pi \int_0^\infty \left(\exp\left(-\frac{u_{ij}(r_{ij})}{k_\mathrm{B}T} \right) - 1 \right) r_{ij}^2 \, \mathrm{d}r \ . \tag{7}$$

From either Eq. (6) or (7), the second virial coefficient is determined as a function of the temperature $B(T)$. From these results, the three characteristic temperatures are determined that correspond to the zero-density limit state points of the four characteristic curves – the Boyle and the Zeno curve have a common zero-density limit (cf. Fig. 1). The three characteristic virial coefficient points are:[3,5] $B = 0$, $B = B_\mathrm{max}$, and $\partial B/\partial T = B/T$, which correspond to the four characteristic temperatures $T_\mathrm{limit,Z} = T_\mathrm{limit,B}$, $T_\mathrm{limit,A}$, and $T_\mathrm{limit,C}$, respectively (cf. Fig. 1).

For applying Eq. (6), MC simulations are carried out in a wide temperature range and the characteristic virial coefficient points are determined by interpolation. For applying Eq. (7), a Newton solver is applied to directly solve the conditions for the characteristic virial coefficient points. Hence, while small statistical uncertainties apply to the simulation route using Eq. (6), practically no uncertainties apply to the direct potential evaluation route using Eq. (7). For the latter, the zero-density limit characteristic curve state point results are exact (within the significant digits used for the computer precision calculations).

In this work, Eq. (6) was applied for the evaluation of the toluene, ethane, propane, and ethanol force field using MC simulations in *ms*2 (see Ref.[24] for details), whereas Eq. (7) was applied for the evaluation of the LJ and LJTS potential.

The zero-density limit characteristic curve temperatures $T_{\mathrm{limit},\hat{i}}$ with $\hat{i} = Z, A, B, C$ obtained from the virial route are used to correct the EOS initial guess values. Thereby, the virial-corrected characteristic curve temperatures $\underline{T}_{\hat{i}}^\mathrm{corr}$ are calculated as

$$\underline{T}_{\hat{i}}^\mathrm{corr} = \underline{T}_{\hat{i}}^\mathrm{EOS} + 0.5\Big(1 + \tanh\left(K_{\hat{i}}(\underline{T}_{\hat{i}}^\mathrm{EOS} - 0.95\, T_{\mathrm{limit},\hat{i}}^\mathrm{virial})\right)\Big)(T_{\mathrm{limit},\hat{i}}^\mathrm{virial} - T_{\mathrm{limit},\hat{i}}^\mathrm{EOS}) \ , \tag{8}$$

where $\underline{T}_{\hat{i}}^\mathrm{EOS}$ indicates the vector of temperature values predicted by the EOS for a given

characteristic curve $\hat{i} = Z, A, B, C$ and $\underline{T}_{\hat{i}}^{\mathrm{corr}}$ indicating the virial-corrected vector of temperature values. The temperatures $T_{\mathrm{limit},\hat{i}}^{\mathrm{EOS}}$ and $T_{\mathrm{limit},\hat{i}}^{\mathrm{virial}}$ indicate the zero-density limit values obtained from the EOS and the virial route, respectively. Based on Eq. (8), the temperature of a given characteristic curve is shifted by $T_{\mathrm{limit},\hat{i}}^{\mathrm{virial}} - T_{\mathrm{limit},\hat{i}}^{\mathrm{EOS}}$ starting at 95% of the zero-density limit temperature. This shift is only applied in the vicinity of the zero-density limit using a tanh function. Thereby the virial-corrected initial guess values are continuous and exhibit the force field zero-density limit. The parameter $K_{\hat{i}}$ in Eq. (8) is calculated by

$$K_{\hat{i}} = \frac{2.647}{T_{\mathrm{limit},\hat{i}}^{\mathrm{EOS}} - 0.95\, T_{\mathrm{limit},\hat{i}}^{\mathrm{virial}}} \tag{9}$$

to scale the tangent hyperbolic function.

Setup of the Simulations

Based on the virial coefficient-corrected EOS initial guess data, the simulation state point grid is generated. In general, the simulations can be carried out in different ensembles. Here, the NVT and NpT ensemble are considered. Based on the ensemble used in the simulations, the grid has to be specified such that the simulations from a set have the same thermodynamic variable X. Fig. 3 schematically shows the simulation grid configurations considered in this work. The simulations used for determining one characteristic curve state point are thereby specified either at isothermal, isochoric, or isobaric conditions. Moreover, a method is tested where the sets of simulation state points are approximately orthogonal to the respective characteristic curve in either the density-temperature or pressure-temperature projection. This "gradient" method can only be used to evaluate conditions which are not linked to an iso-condition, e.g. for the compressibility factor condition $Z = 1$.

Most simulation grid types depicted in Fig. 3 can be combined with the different thermodynamic characteristic curve conditions (cf. Table 1). However, not all combinations of simulation grid and thermodynamic condition are feasible, e.g. the evaluation of a derivative

at isochoric conditions requires an isochoric arrangement of the simulation set. Table 2 summarizes the simulation settings considered in this work for all four characteristic curves. For a given characteristic curve, the initial guess value was the same for all studied simulation settings, cf. Table 2.

The simulation grid is generated based on a heuristic function depending on both the temperature and the distance to specific points, e.g. the zero-density limit and the critical point (cf. Fig. 3). Details on the grid generator are given in the Supporting Information. Simulations in the unstable region (as predicted by the EOS) are circumvented. Also, the large difference of the compressibility of the fluid in the different state regions is considered by the grid generator such that the characteristic curve state points can be determined with high accuracy. The grid generator covers three orders of magnitude in pressure and two orders of magnitude in temperature and, moreover, covers the metastable VLE and SLE region.

The grid generator has some method-specific parameters such as the number of state points N_{sim} used in a simulation set, the number of simulation sets N_{set} (corresponding to the number of characteristic curve state points to be determined), and the parameter L characterizing the scattering width of the data points of a simulation set around the initial guess value (see Supporting Information for details). The simulation parameters are recommended to be in the range N_{sim} = 5...10, N_{set} = 10...30, and L_{NVT} = 0.02...0.03 for NVT and L_{NpT} = 0.05...0.08 for NpT simulations.

Molecular Simulations

Simulation Settings

Molecular dynamics simulations are carried out at each state point on the simulation grid. The simulations are carried out either in the NVT or NpT ensemble (cf. Table 2). For the barostat, the piston mass parameter M_{piston} is to be specified carefully such that a stable simulation is carried out at each state point. This is not trivial as a large pressure and

temperature range is covered by the simulations. The piston mass parameter is given in the dimension of kg/m^4. Based on preliminary simulations, a simple heuristic function was developed that describes the barostat piston mass parameter M_{piston} as a function of the temperature and pressure as

$$M_{\mathrm{piston}} = 10^{-7}\left(10^{\frac{1}{3}\log_2(\frac{p}{10p_\mathrm{c}})-\frac{1}{4}\log_2(\frac{T}{2.5T_\mathrm{c}})}\right)\frac{\mathrm{kg}}{\mathrm{m}^4}\ , \tag{10}$$

where T_c and p_c indicate the critical temperature and pressure, respectively.

For the sampling of the Helmholtz energy derivatives, the *Lustig* formalism[26–28] is applied. Thereby, the Helmholtz energy derivatives up to second order are directly sampled in the NVT simulation from the fluctuation theorem. Based on this data, the Helmholtz energy derivative conditions of the characteristic curves are applied, cf. Table 1.

Fig. 4 shows the relations of the thermodynamic properties sampled in *ms*2 that are used in this work for the different characteristic curve conditions, cf. Table 1. The left column indicates the primary variables sampled in the simulation, i.e. the velocity, potential energy, and coordinates of the particles as well as the box volume. The blue highlighted variables in Fig. 4 indicate the properties used for evaluating the different thermodynamic conditions (cf. Table 1). As the sampling of these properties in the simulation goes hand in hand with different degrees of noise, i.e. yield in general different accuracy and precision, it is a main goal of this work to determine the most beneficial sampling route.

In this work, the system size of the MD simulations was 2,500 particles. The time step was $\delta\tau = 0.001\,\sigma\sqrt{m/\varepsilon}$ for the Lennard-Jones model fluid simulations. The equilibration was carried out for 50,000 time steps in the NVT ensemble and additional 50,000 time steps in the NpT ensemble if production was carried out in the NpT ensemble. The number of production steps was 750,000. The cut-off radius was $5\,\sigma$ for the full Lennard-Jones fluid and in the case of the LJTS fluid, the cut-off was $2.5\,\sigma$.[21] For the real substance fluids, the time step was set to $\delta\tau = 2.3\,\mathrm{fs}$ for toluene, ethane, and propane and $\delta\tau = 1.16\,\mathrm{fs}$ for

ethanol. The cut-off radius was $r_c = 15\,\text{Å}$ for the real substance simulations. For the cut-off radius, the center of mass method was used. For the electrostatic long-range interactions, the reaction field method was used. Classical velocity scaling was applied for thermostating and the Anderson barostat for prescribing the pressure.

Determining Characteristic Curve State Points

Based on the respective thermodynamic condition (cf. Table 1), the results from each simulation set are evaluated to determine a characteristic curve state point. Therefore, a second-order polynomial function is fitted to the simulation results, cf. Fig. 5-left. Then, the function is evaluated such as the state point is determined that fulfills the thermodynamic condition for a given characteristic curve.

For determining the characteristic curve state points from the respective thermodynamic condition, one of two procedures is applied: (1) a thermodynamic property W directly sampled in the simulation is to be equal to zero or unity – depending on the condition; (2) the derivative of a thermodynamic property W with respect to a state variable Y is to be equal to zero. The procedure (1) applies to the four Helmholtz energy derivative conditions (green labeled line in Table 1), the condition $Z = 1$ for the Zeno curve, and the two derivatives $(\partial u/\partial v)_{T,ms2}$ and $(\partial h/\partial p)_{T,ms2}$ (directly sampled by $ms2$). The procedure (2) applies to all remaining thermodynamic conditions considered in this work (cf. Table 1). For procedure (1) cases, the zero (or unity) crossing point of the fitted curve determines the characteristic curve state point regarding Y. For procedure (2) cases, the minimum of the fitted curve determines Y. Examples for the fits to the simulation results for all considered routes (cf. Table 1) are presented in the Supporting Information. From the evaluation of the simulation set results, each characteristic curve state point is sufficiently specified by two independent thermodynamic state variables X and Y. One state variable X was prescribed as boundary condition and one variable Y is determined from the fitting procedure. The remaining variable Z (out of pvT) is – as an intermediate step – estimated by a cubic interpolation

with not-a-knot end conditions between the results of the simulation set. The full set of the three state variables pvT at a given characteristic curve state point is determined in an independent simulation, see below.

Statistical Uncertainties

The results for the characteristic curve state points are subject to uncertainties. Such arise from the molecular simulations themselves, the quality of the fitting procedure described above, and the quality of the initial guess values. Here, a new method for estimating the statistical uncertainties is proposed. Thereby, both the uncertainties from the simulations as well as those from the fitting procedure are considered. The uncertainty estimation method – termed *error ellipse method* – is schematically shown in Fig. 5. Therein, the error ellipse method is demonstrated on procedure (2) type data. Hence, the derivative of a given property W with respect to a given state property Y is to fulfill the condition $\partial W/\partial Y = 0$. Both properties W and Y are subject to statistical uncertainties due to the numerical nature of the molecular simulation. The statistical uncertainties δW_{mn} and δY_{mn} are obtained from the individual simulations with $m = 1...N_{\mathrm{set}}$ and $n = 1...N_{\mathrm{sim}}$. In this work, the statistical uncertainties δW_{mn} and δY_{mn} were computed in $ms2$ using the classical block averaging method.[41]

To determine the statistical uncertainty of the characteristic curve state point δY_m, an ensemble N_{fit} of worst case fits is evaluated. Therefore, an ellipse for each simulation result data point (W_{mn}, Y_{mn}) is computed with the semi-major and semi-minor axes being the statistical uncertainty of the data point δW_{mn} and δY_{mn}, cf. Fig. 5-left. By randomly selecting a set of points on the ellipsis of the data points of a simulation set, a pseudo data point set is generated (green data points in Fig. 5-left). For the pseudo data point set, the fitting procedure (as described above) is applied again. From that fit, a new pseudo characteristic curve state point Y'_{mo} is determined with $o = 1...N_{\mathrm{fit}}$. The standard deviation

is then computed as

$$\delta Y_m = \sqrt{1/N_{\mathrm{fit}} \sum_{o=1}^{N_{\mathrm{fit}}} \left(Y'_{mo} - \left(1/N_{\mathrm{fit}} \sum_{o=1}^{N_{\mathrm{fit}}} Y'_{mo} \right) \right)^2} \,. \tag{11}$$

This procedure is repeated N_{fit}-times until the standard deviation δY_m converges, cf. Fig. 5-right. As a criterion for convergence, the fluctuation of δY_m is to decay below 1% over the previous 50 evaluation steps.

Simulations at Characteristic Curve State Points

For each determined characteristic curve state point, an additional NVT MD simulation is carried out. This is done for two reasons: (a) to fully determine the thermodynamic characteristic curve state point pvT (one of the three variables is only known by spline interpolation of the sample points of the simulation set) and (b) to apply the *Lustig* formalism[26–28] such that $\tilde{a}_{kl}$ with $k, l = 1, 2$ are determined at the characteristic curve state points. Thereby, the characteristic curve state points can be assessed regarding their thermodynamic consistency using the Helmholtz energy derivative conditions, cf. Table 1. Moreover, a large number of thermodynamic properties at the characteristic curve state points becomes available. The simulation settings are equal to the NVT simulation settings described above.

Compiling Results and Assessment of Thermodynamic Consistency

In a final step, the results are compiled and assessed regarding the thermodynamic consistency. For the data compilation, the zero-density characteristic curve state points obtained from the virial route are added to the molecular simulation results obtained from the grid evaluation. For the latter, the statistical uncertainties were determined from the error ellipse method, whereas practically no uncertainties apply for the zero-density characteristic curve state points.

Three consistency tests are applied to the final data set: (1) for each characteristic curve,

the data points obtained from molecular simulations at low densities are compared to the zero-density limit data points obtained from the virial coefficient route. The latter has – especially in the case of simple model fluids – a significantly higher precision and accuracy. Hence, the molecular simulation results at low densities are to converge into the zero-density limit data to be thermodynamically consistent. (2) The Helmholtz energy derivative data $\tilde{a}_{kl}$ sampled at a given characteristic curve state point is used to validate the thermodynamic condition for the characteristic curve (cf. green colored line in Table 1). (3) It is verified that the molecular simulation characteristic curve results comply with the regularities postulated by *Brown.*[1]

Implementation

The computational procedure outlined above for determining Brown's characteristic curves is available in the electronic Supporting Information as a script-based implementation of the algorithm. These workflow manager scripts are written in Matlab and shell. The presented implementation contains functions for pre-processing, post-processing, and the evaluation of the three simulation steps. The implementation of the algorithm is depicted in Fig. 6. The implementation enables a highly automated execution of the entire algorithm (cf. Fig. 2). Thereby, the three simulation steps are subsequently carried out: (1) the calculation of the virial coefficient, (2) the determination of the characteristic curve state points, and (3) a final simulation at the estimated characteristic curve state points. In each of these simulation steps, the workflow manager can be used for four main tasks: (1) to create the input files for the simulations, (2) to launch the simulations on a given cluster machine, (3) to carry out the post-processing, and (4) to perform the physical evaluation of the results. Accordingly, the main part of the workflow manager consists of four functions: `PreProcessing.m`, `CreateParFiles.sh`, `PostProcessing.m`, and `Evaluation.m`. Since these four tasks are similar for the three simulations, the workflow manager was efficiently implemented in four functions that are used in each simulation step. The simulation step is specified by the user

via the argument `MODE`, cf. Fig. 6.

Both, the SI units system and the Lennard-Jones units system are implemented in the workflow manager. The SI units system can be favorably used for real substances, e.g. toluene, whereas the reduced units system can be favorably used for model substances such as the Lennard-Jones fluid[14] or the 2CLJQ model system.[42,43] The user can specify the desired units system via the `UNITS` argument in the function call.

The implementation was used in this work in conjunction with *ms*2,[15] but it can be straightforwardly adapted to other simulation engines. The force field input files can be directly taken from the MolMod database.[16] Thereby, the implementation presented here can be flexibly integrated in different user workflows.

The workflow has some simulation parameters, e.g. for specifying the number of temperatures to be evaluated for the second virial coefficient, the number of simulations in a simulation set N_{sim}, and the number of sets N_{set} for a given characteristic curve. Details on the simulation parameters of the workflow manager are given in the Supporting Information.

Comparison of Sampling Methods

For each of the four characteristic curves, multiple sampling approaches were tested in this work (all available in the implementation). Table 2 gives an overview of all tested approaches, which were applied to the Lennard-Jones fluid and toluene. For the Zeno and the Boyle curve, six approaches were compared; seven approaches for the Amagat; and eight approaches for the Charles curve. Each approach consists of a thermodynamic condition (cf. Table 1) and a simulation grid type (cf. Fig. 3).

To identify the most favorable approach for each curve, the following criteria were used in the comparison: (i) the scattering of the determined characteristic curve state points, (ii) the magnitude of the statistical uncertainty δY, (iii) the quality of the fit curves, (iv) the behavior of the results in the low-density region and their consistency with the zero-density

limit data point, (v) the behavior of the results at low temperatures in the vicinity of the VLE binodal and in the VLE metastable region, (vi) the behavior of the results in the high-density region in the vicinity of the solid-fluid equilibrium, (vii) the complexity of the grid, (viii) the computational complexity of the molecular simulation method, (ix) the accessibility of the required properties, and (x) the required simulation time. Based on this systematic evaluation, for each characteristic curve, the most beneficial approach was identified.

Based on the comprehensive study on the Lennard-Jones fluid and toluene, the most favorable sampling route was identified among several ones that were considered, cf. Table 2. The results for the Lennard-Jones fluid are discussed in detail in the main body of this work. The results for toluene are in most parts presented in the Supporting Information. The findings reported in the Supporting Information for toluene support the findings reported here for the Lennard-Jones fluid regarding the benefits and drawbacks of the different sampling routes. Finally, the most favorable sampling route was applied to determine the characteristic curves of ethane, propane, and ethanol. The final results of these are presented in the main body of this work and confirm the robustness of the determined sampling approach. Details are reported in the Supporting Information.

For the graphical representation of the results, a consistent color and symbol code was used. The symbol color thereby indicates the thermodynamic condition applied in the data set (cf. Table 1) and the symbol type indicates the grid type (cf. Fig. 3).

For all four characteristic curves, the Lennard-Jones fluid results from all tested sampling routes are presented and discussed in both the pressure-temperature and density-temperature projection – including the corresponding deviation plots. The corresponding toluene results are given in the Supporting Information. Also, the (uncorrected) initial guess equation of state data are shown. The shown error bars are obtained from the error ellipse method.

Zeno Curve

Fig. 7 shows the results for the Zeno curve of the Lennard-Jones fluid. Overall, the results from the different methods are in very good agreement. The results from this work deviate from the results from *Deiters & Neumaier*[6,14] – in particular in the vicinity of the pressure maximum of the Zeno curve. However, no uncertainties were reported for this data set.[6,14] Also, only the pressure-temperature data is available for this data set.[6,14]

The data sets from all approaches obtained in this work show very small scattering in a wide temperature range. Nevertheless, in the vicinity of the zero-density limit, the results from all approaches show significant scattering. All methods have similarly small error bars, which however increase upon approaching the zero-density limit. The NpT simulations yield slightly smaller error bars in the low-temperature region. The quality of the results of the fit curves (presented in the Supporting Information) is overall similar for the different approaches. In the vicinity of the zero-density limit, all data sets show an increasing scattering. In the high-density region, the data points from the "Z = 1 NVT gradient" data set exhibit larger scattering compared to the results from other approaches. Regarding the complexity of the grid, placing the simulation points perpendicular to the curve predicted by the EOS does not provide significant improvements. Therefore, the simple isothermal arrangement is preferred. Regarding the computational complexity, only the NpT simulations are slightly more demanding due to the barostat and the additional simulation settings required for the piston mass parameter. Also, the NpT simulations required about 7% more computer time compared to the NVT simulation (due to the additional NpT equilibration and the barostating). Overall, the approach "Z = 1 NVT isothermal" is found to be most beneficial for determining the Zeno curve.

The Zeno curve exhibits the peculiarity that it exhibits a linear trend in the density-temperature projection. This has been discovered by *Batschinski*[44] and more recently studied by *Apfelbaum et al.*[45,46] for different substances. The applicability of this linearity-law was tested here based on the simulation data from this work. The results presented in the

Supporting Information show that the computer experiment results are in good agreement with the linearity-law, but not exact.

Amagat Curve

The results for the Amagat curve are shown in Fig. 8. The results from the different approaches do not agree as well as for the Zeno curve. However, for the Amagat curve, the results from *Deiters & Neumaier*[6,14] agree with the results from this work within the scattering and the uncertainties. The first three data points from *Deiters & Neumaier*[6] are probably located in the metastable solid-fluid region.[3]

The results obtained from the $\tilde{a}_{11} = 0$ route and the $(\partial Z/\partial T)_v = 0$ route show some scattering, whereas the results obtained from the $(\partial u/\partial v)_T = 0$ route are relatively smooth. Also, the results from the routes $\tilde{a}_{11} = 0$ and $(\partial Z/\partial T)_v = 0$ yield larger statistical uncertainties, which is due to the fact that the simulation results for a given set of state points exhibit some scattering and the fitted polynomial curves cannot describe the data perfectly (see Supporting Information for details). Both $(\partial u/\partial v)_T = 0$ data sets are in excellent agreement with the zero-density limit data point, whereas the other data sets show important scattering in the vicinity of the zero-density limit. Comparing the two $(\partial u/\partial v)_T = 0$ data sets in the low-temperature region, freezing was observed in the NVT simulations for the last data points (not shown in Fig. 8), whereas for the NpT simulations, freezing in the metastable region was only observed for the lowest studied temperature. Hence, the NpT simulations are more beneficial for studying the solid-liquid metastable region of the Amagat curve. For the Amagat curve, the NVT ensemble simulations are computationally less expensive, i.e. they require on average 8% less computer time than the NpT simulations.

The simulation engine used in this work directly samples $(\partial u/\partial v)$ in NVT simulations. This data was also used for computing the characteristic curve state points. The results are only presented in the Supporting Information as they exhibit significantly larger scattering and statistical uncertainties compared to the results obtained form the evaluation of

$(\partial u/\partial v)_T = 0$ taking u and v sampled in the simulations.

Overall, for determining the Amagat curve, the method "$(\partial u/\partial v)_T = 0$ NpT isotherm" is found to be most beneficial.

Boyle Curve

Fig. 9 shows the results for the Boyle curve. The results from this work agree reasonably well with the results from *Deiters & Neumaier*.[6,14] The results obtained from the Helmholtz energy route $\tilde{a}_{01} + \tilde{a}_{02} = 0$ show large scattering compared to the other approaches. The four data sets from the compressibility factor routes (two from the $(\partial Z/\partial p)_T = 0$ route and two from the $(\partial Z/\partial v)_T = 0$ route) are in excellent agreement in a wide temperature range. The zero-density limit is captured very well by all four compressibility factor route data sets. Nevertheless, in the vicinity of the vapor-liquid equilibrium, important deviations are observed: interestingly, the results obtained from the $(\partial Z/\partial p)_T = 0$ route significantly deviate – especially in the ρ-T projection – from the $(\partial Z/\partial v)_T = 0$ results and the EOS initial guess value (which is known to give a realistic description of that fluid region[47]). The results of the fit curves for the "$(\partial Z/\partial p)_T = 0$ NVT isotherm" data set (see Supporting Information) reveal that the second order polynomial does not describe the simulation results well at low temperatures. The results of the fit curves for the "$(\partial Z/\partial p)_T = 0$ NpT isotherm" data set indicate that several simulations already contained a vapor phase, which was confirmed by an inspection of the simulation trajectories. The same was observed for the "$(\partial Z/\partial v)_T = 0$ NpT isotherm" simulations at low temperatures, but the effect has only a minor influence on the determined state point. In the low-temperature region, only the "$(\partial Z/\partial v)_T = 0$ NVT isotherm" data set yields reliable results with low scattering. The "$(\partial Z/\partial v)_T = 0$ NVT isotherm" route is also most beneficial regarding the computational complexity, the grid complexity, and the computational effort. Hence, the "$(\partial Z/\partial v)_T = 0$ NVT isotherm" route is overall found to be the most favorable route for determining the Boyle curve.

Charles Curve

Fig. 10 shows the results for the Charles curve. Opposite to the Zeno, Amagat, and Boyle curve, several data sets are available in the literature for the Lennard-Jones fluid Charles curve.[6–8,10,48–50] The results from the literature overall exhibit significant scattering (discussed in detail in the Supporting Information). The results from this work agree with the literature results within this scattering range.

For both isobaric approaches, no results near the pressure maximum can be determined, which is simply due to the fact that the minimum of $(\partial Z/\partial T)_p$ cannot be reliably determined from the seven simulation points. Moreover, the uncertainties of the results from the isobaric approaches increase upon approaching the pressure maximum. Also, the results from the isobaric approaches exhibit significant scattering in the vicinity of the zero-density limit. The results from the Helmholtz energy derivative route show important scattering in the entire temperature range, which also goes hand in hand with large statistical uncertainties. The quality of the fit curves (see Supporting Information) is significantly better for the two $(\partial h/\partial p)_T = 0$ data sets compared to the results from the other approaches. Moreover, the results from the $(\partial h/\partial p)_T = 0$ route are in excellent agreement with the zero-density limit characteristic curve state point and show an overall very smooth trend in the entire temperature range. The quality of the two data sets "$(\partial h/\partial p)_T = 0$ NVT isotherm" and "$(\partial h/\partial p)_T = 0$ NpT isotherm" is similar. Since the NVT simulations are computationally less complex and less expensive, the approach "$(\partial h/\partial p)_T = 0$ NVT isotherm" is identified to be the most favorable route for determining the Charles curve.

The simulation engine used in this work directly samples $(\partial h/\partial p)$ in NpT simulations. These data were also used for computing the characteristic curve state points. The results are only presented in the Supporting Information as they exhibit significantly larger scattering and statistical uncertainties compared to the results obtained form the evaluation of $(\partial h/\partial p)$ taking h and p sampled in the simulations.

Assessment of Thermodynamic Consistency

The thermodynamic consistency of the results from the most favorable approaches for determining the four characteristic curves was assessed. Therefore, an additional NVT simulation was carried out at the determined state point. Fig. 11 shows the results for the Helmholtz energy condition sampled in the final MD simulations. Most data points satisfy the respective criterion within their statistical uncertainties. Fig. 12 shows the final results of the four characteristic curves (for both the Lennard-Jones fluid and toluene). For the Lennard-Jones fluid results, the criteria postulated by Brown are well satisfied, e.g. regarding the curvature, maxima, intersection points etc. Moreover, the final MD results are consistent with the zero-density limit data points obtained from the virial route. Also, the toluene results are conform with Brown's criteria and the zero-density limit data points. More details on the toluene results are given in the Supporting Information.

Determining the Characteristic Curves of Methane, Ethane, Propane, and Ethanol

The robustness and applicability of the computational procedure was further tested by determining the characteristic curves of methane, ethane, propane, and ethanol. For methane, the Lennard-Jones fluid results were used. For ethane, propane, and ethanol, only the most favorable sampling route was applied. The results for the three n-alkanes are depicted in Fig. 13. The results for ethanol are depicted in Fig. 14. The results from the grid simulations are in excellent agreement with the zero-density limit data point obtained from the virial route – for all studied real substances. The results for the Helmholtz energy consistency test are presented in the Supporting Information. The vast majority of data points is in reasonable accordance with this consistency test. Moreover, the simulation results for all studied real substances are conform with Brown's criteria. Interestingly, the EOS initial guess values of ethanol (cf. Fig. 14) obtained from the SAFT-VR Mie model show some deficiencies, i.e. an undulation for the Charles and Amagat curve. This is not the case for the three studied alkanes. From a model perspective, the main difference between the alkanes and ethanol is

that the association SAFT term was used in the latter. Yet, the computational procedure is sufficiently robust such that characteristic curve state points were reliably determined in the entire state range.

Based on the results for the three studied n-alkanes (cf. Fig. 13), the influence of the chain length on Brown's characteristic curves can be discussed: the overall shape does not change with increasing alkane chain length, which is captured by both the simulation results and the EOS. With increasing chain length, the zero-density limit data point is shifted to higher temperatures. This is in line with the behavior of the critical point. The pressure maximum value is not affected as strongly by the chain length.

Conclusions

In this work, a method for determining Brown's characteristic curves by molecular simulation was developed and tested. The method is generalized such that it can be applied to an arbitrary force field of a molecular fluid. Initial guess values are taken from a molecular-based equation of state. At the core of the computational procedure lies a three-stage molecular simulation sequence: first, the second virial coefficient is sampled in a Monte Carlo run. Second, simulations are carried out on a grid of state points (derived from the virial-corrected EOS initial guess data). From the results, characteristic curve state points are determined. Third, a final simulation at the determined state point is carried out. Finally, the results are assessed regarding the thermodynamic consistency.

For each characteristic curve, different simulation routes were systematically tested and compared. The tests were carried out for two fluids, the Lennard-Jones fluid and toluene. From this systematic comparison, for each characteristic curve, the most beneficial approach was identified that yields reliable results in the entire temperature range. The four most beneficial approaches are:

- $Z = 1$ in NVT simulations for the Zeno curve,

- $(\partial u/\partial v)_T = 0$ in NpT simulations for the Amagat curve,
- $(\partial Z/\partial v)_T = 0$ in NVT simulations for the Boyle curve, and
- $(\partial h/\partial p)_T = 0$ in NVT simulations for the Charles curve.

Moreover, the method was further tested on ethane, propane, ethanol, and the Lennard-Jones truncated & shifted fluid. The results support the robustness and general applicability of the approach.

An implementation of the developed algorithm is provided as an automated workflow manager tool. Despite the fact that the tool was used in combination with the simulation engine *ms*2 in this work, the implementation can readily be used with other simulation engines.

Based on the computational procedure and tool developed in this work, reliable predictions for Brown's characteristic curves can be obtained for a given force field model, which can then be used for testing the extrapolation behavior of equations of state. In this work, rigid united-atom force fields for relatively small molecules were used. For future work, it would be interesting to compare different force field types, e.g. all-atom, coarse grain, and reactive force fields. Moreover, classical Lennard-Jones force fields were used here, which have the repulsive exponent conveniently chosen as 12, which is known to be problematic – especially at elevated pressure. Hence, it would be interesting to study Brown's characteristic curves of the Mie potential, which is known to provide a more accurate description of the repulsive interactions of real fluids.

Conflicts of Interest

There are no conflicts of interest to declare.

Acknowledgement

The authors gratefully acknowledge financial support by the Deutsche Forschungsgemeinschaft (DFG) within the IRTG 2057 Physical Modelling for Virtual Manufacturing Systems and Processes (project number 252408385), by the BMBF within the WindHPC project, and by the KSB foundation. The simulations were carried out on the ELWE supercomputer at Regional University Computing Center Kaiserslautern (RHRK) under the grant TUK-MTD.

Supporting Information Available

Tables & figures

Table 1: Thermodynamic conditions of the four characteristic curves. The color bar indicates thermodynamic conditions considered in this work. The color bar corresponds to the color code used in the plots. The approach identified as the most favorable one is colored in gray.

	Zeno (Z)	Amagat (A)	Boyle (B)	Charles (C)
	$\tilde{a}_{01} = 0$	$\tilde{a}_{11} = 0$	$\tilde{a}_{01} + \tilde{a}_{02} = 0$	$\tilde{a}_{01} + \tilde{a}_{02} + \tilde{a}_{11} = 0$
	$Z = 1$	$\left(\frac{\partial Z}{\partial T}\right)_v = 0$	$\left(\frac{\partial Z}{\partial p}\right)_T = 0$	$\left(\frac{\partial Z}{\partial T}\right)_p = 0$
		$\left(\frac{\partial u}{\partial v}\right)_T = 0$	$\left(\frac{\partial Z}{\partial v}\right)_T = 0$	$\left(\frac{\partial Z}{\partial v}\right)_p = 0$
				$\left(\frac{\partial h}{\partial p}\right)_T = 0$
[A]		$\left(\frac{\partial u}{\partial v}\right)_{T,ms2} = 0$		$\left(\frac{\partial h}{\partial p}\right)_{T,ms2} = 0$
		$\left(\frac{\partial p}{\partial T}\right)_v = \frac{p}{T}$	$\left(\frac{\partial p}{\partial v}\right)_T = -\frac{p}{v}$	$\left(\frac{\partial v}{\partial T}\right)_p = \frac{v}{T}$
				$\left(\frac{\partial T}{\partial p}\right)_h = 0$

[A] Derivatives sampled directly by the molecular simulation engine *ms2*.

Table 2: Considered computational approaches for determining the characteristic curves: Zeno (Z), Amagat (A), Boyle (B), and Charles (C). All combinations of thermodynamic condition (cf. Table 1) and simulation grid type (cf. Fig. 3) considered in this work. The approach identified as the most favorable one is colored in gray.

	condition	grid		condition	grid
Z	$\tilde{a}_{01} = 0$	NVT isotherm	B	$\tilde{a}_{01} + \tilde{a}_{02} = 0$	NVT isotherm
	$\tilde{a}_{01} = 0$	NVT gradient		$\tilde{a}_{01} + \tilde{a}_{02} = 0$	NVT gradient
	$Z = 1$	NVT isotherm		$(\frac{\partial Z}{\partial p})_T = 0$	NVT isotherm
	$Z = 1$	NVT gradient		$(\frac{\partial Z}{\partial p})_T = 0$	NpT isotherm
	$Z = 1$	NpT isotherm		$(\frac{\partial Z}{\partial v})_T = 0$	NVT isotherm
	$Z = 1$	NpT gradient		$(\frac{\partial Z}{\partial v})_T = 0$	NpT isotherm
A	$\tilde{a}_{11} = 0$	NVT isotherm	C	$a_{01} + \tilde{a}_{02} + \tilde{a}_{11} = 0$	NVT isotherm
	$\tilde{a}_{11} = 0$	NVT gradient		$\tilde{a}_{01} + \tilde{a}_{02} + \tilde{a}_{11} = 0$	NVT gradient
	$(\frac{\partial Z}{\partial T})_v = 0$	NVT isochor		$(\frac{\partial Z}{\partial T})_p = 0$	NpT isobar
	$(\frac{\partial u}{\partial v})_T = 0$	NVT isotherm		$(\frac{\partial Z}{\partial v})_p = 0$	NpT isobar
	$(\frac{\partial u}{\partial v})_T = 0$	NpT isotherm		$(\frac{\partial h}{\partial p})_T = 0$	NVT isotherm
	$(\frac{\partial u}{\partial v})_{T,ms2} = 0$	NVT isotherm		$(\frac{\partial h}{\partial p})_T = 0$	NpT isotherm
	$(\frac{\partial u}{\partial v})_{T,ms2} = 0$	NVT gradient		$(\frac{\partial h}{\partial p})_{T,ms2} = 0$	NpT isotherm
				$(\frac{\partial h}{\partial p})_{T,ms2} = 0$	NpT gradient

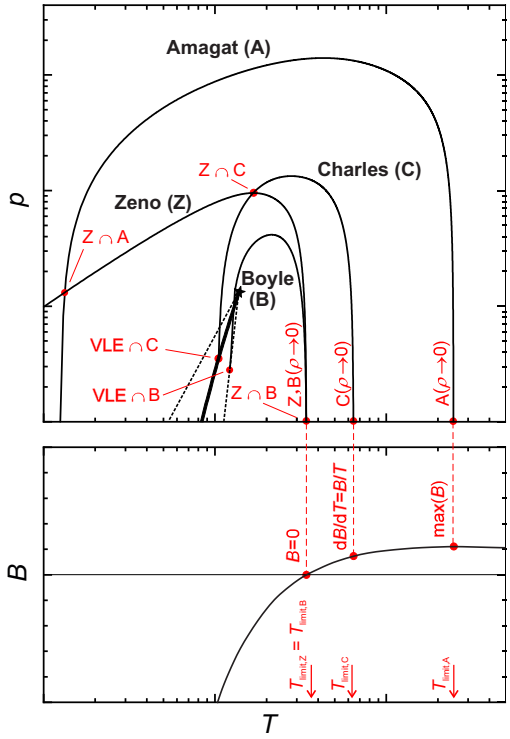

Figure 1: Scheme of Brown's characteristic curves in the double logarithmic pressure-temperature projection (top) and the second virial coefficient (bottom). Red dashed lines indicate the link between the zero-density limit of the characteristic curves and the second virial coefficient. Top plot: thick black line indicates vapor-liquid equilibrium binodal, dashed black lines indicate vapor-liquid equilibrium spinodals, and thin black lines indicate the four characteristic curves. Red symbols indicate characteristic points; the black star indicates the critical point.

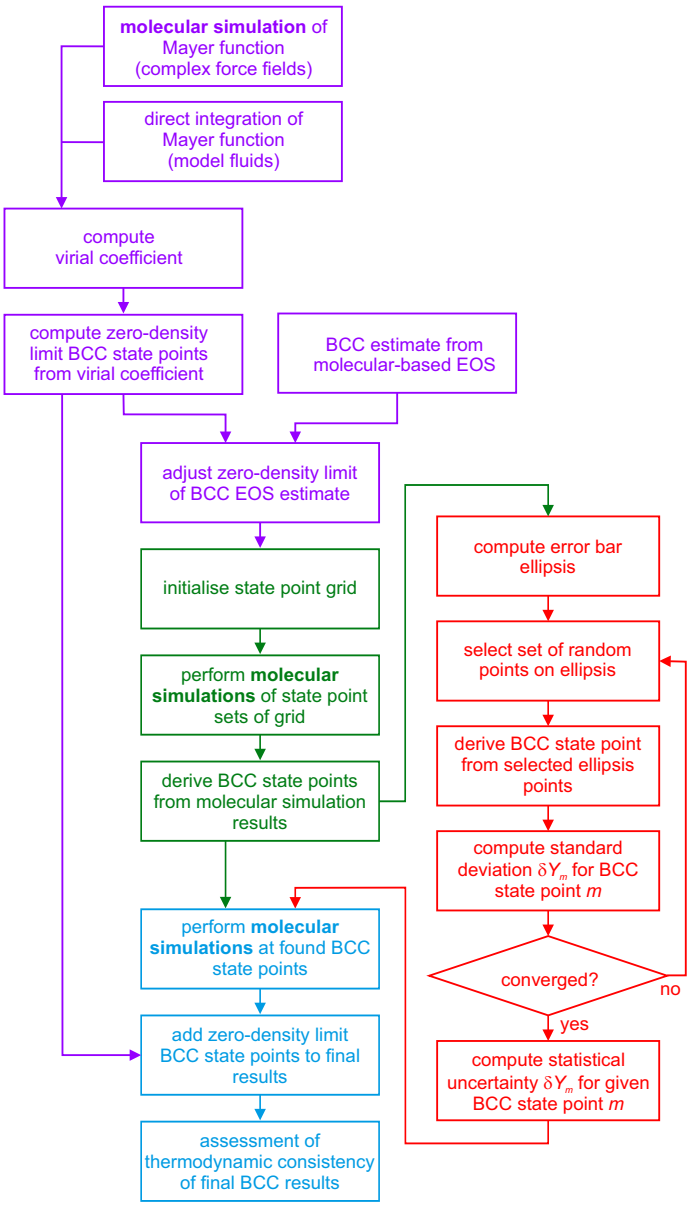

Figure 2: Flowchart of the proposed method for determining Brown's characteristic curves (BCC). Purple indicates the computation of an initial guess of the characteristic curves – including the exact zero-density BCC state points from the virial route. Green indicates the central molecular simulations for determining the characteristic curve state points. Red indicates the calculation of the statistical uncertainty. Blue indicates the data compilation and assessment of the thermodynamic consistency.

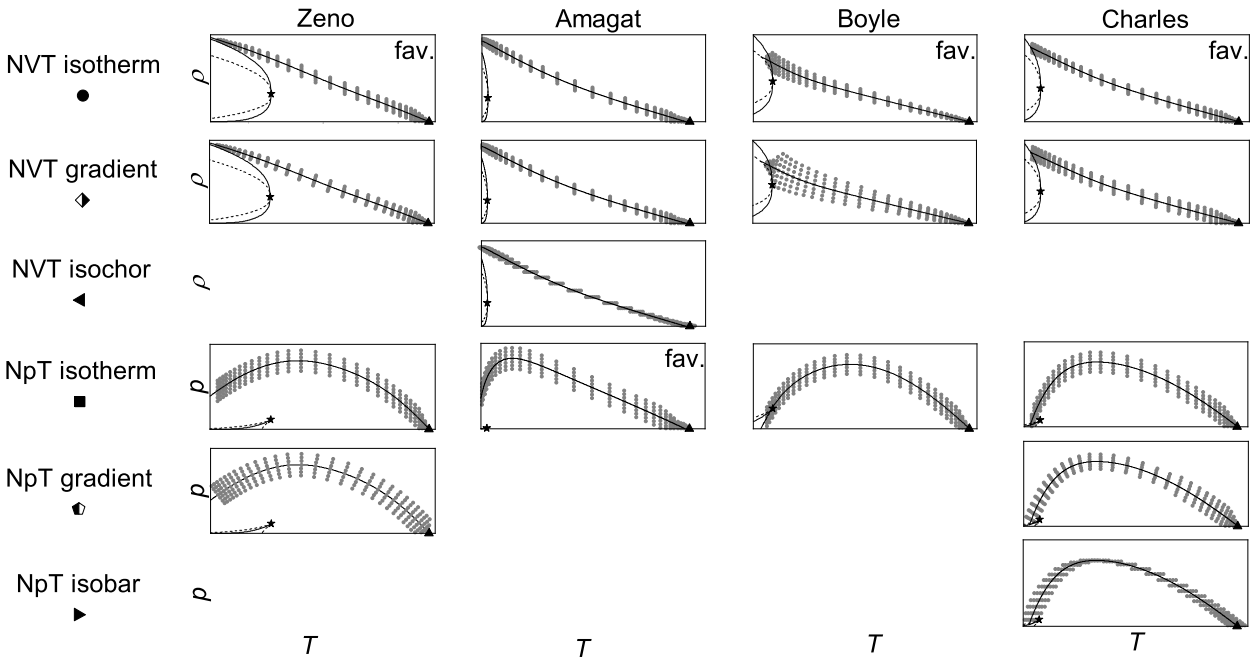

Figure 3: Grid types for simulation sets tested for the four characteristic curves. Gray dots indicate the simulation state points. Black lines and triangles indicate the virial-corrected EOS initial guess. The most favorable grid type identified in this work is indicated by 'fav.'. The black symbol depicted in the first column is consistently used in the following for the respective grid type.

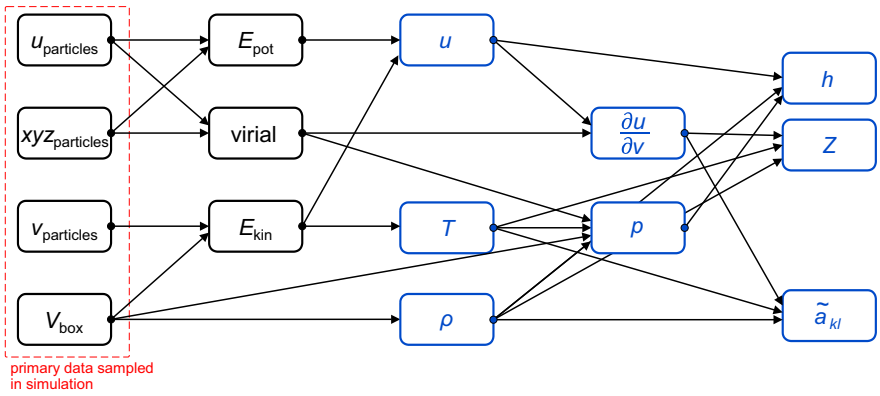

Figure 4: Schematic representation of the relation of the sampled properties (exemplaricly shown for $ms2$ here). The potential energy of the particles $u_{\text{particles}}$, the position of the particles $xyz_{\text{particles}}$, the velocity of the particles $v_{\text{particles}}$, and the volume of the simulation box V_{box} are the primary variables sampled in the simulation. The other thermodynamic properties are derived from these: the potential energy of the system E_{pot}, the virial of the system, the total kinetic energy of the system E_{kin}, the internal energy u, its derivative with respect to volume $\partial u/\partial v$, the pressure p, the enthalpy h, the compressibility factor Z, and the Helmholtz energy derivatives $\tilde{a}_{kl}$. The properties indicated in blue were used in this work for determining the characteristic curves.

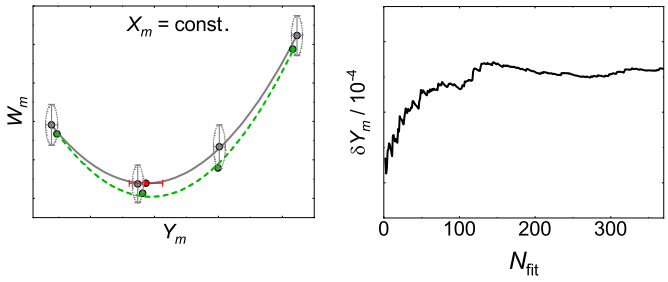

Figure 5: Schematic representation of the fitting method (left) and the convergence of the error ellipse method (right). The fitting method is used to determine the characteristic curve state point m (red point) with respect to the state point variable Y, where Y indicates one of (pvT). The second-order polynomial curve (gray line) was fitted to the results from the set of simulation points with $n = 1...N_{\text{sim}}$ (gray points), which were at constant X, where X indicates one other state variable out of (pvT). For determining the uncertainty δY_m of the characteristic curve state point m, ellipsis were computed from the error bars δW_{mn} and δY_{mn}. Randomly, points on the different ellipsis (green points) were used to re-fit a polynomial curve (green curve) and derive Y'_m. This was repeated $o = 1...N_{\text{fit}}$-times and the standard deviation was computed (cf. Eq. (11)). Once $\delta Y(N_{\text{fit}})$ was converged (right plot), the statistical uncertainty δY_m (red error bar) of the state point variable Y_m was obtained.

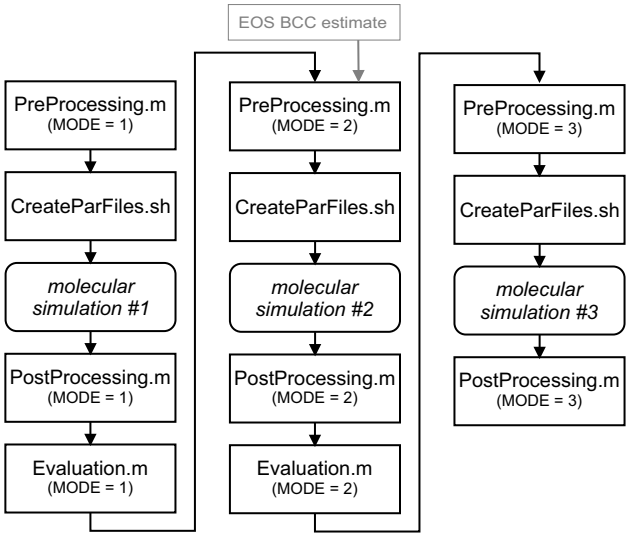

Figure 6: Flowchart of the implementation of the algorithm proposed in this work. The underlying source code files are presented in the Supporting Information. In the first column, molecular simulations are set up, carried out, and evaluated for determining the second virial coefficient and its characteristic points (purple section in Fig. 2). In the second column, molecular simulations are set up (based on the initial guess data from the EOS and the virial coefficient), carried out, and evaluated for determining the characteristic curve state points with respect to two state point variables X, Y (two out of pvT) as well as the statistical uncertainties (green and red sections in Fig. 2). In the third column, molecular simulations are set up, carried out, and evaluated at the determined characteristic state point. Based on that data, the thermodynamic consistency of the results is evaluated (blue section in Fig. 2). The different thermodynamic routes (cf. Fig. 3 and Table 1) can be applied and specified in the implementation by the user.

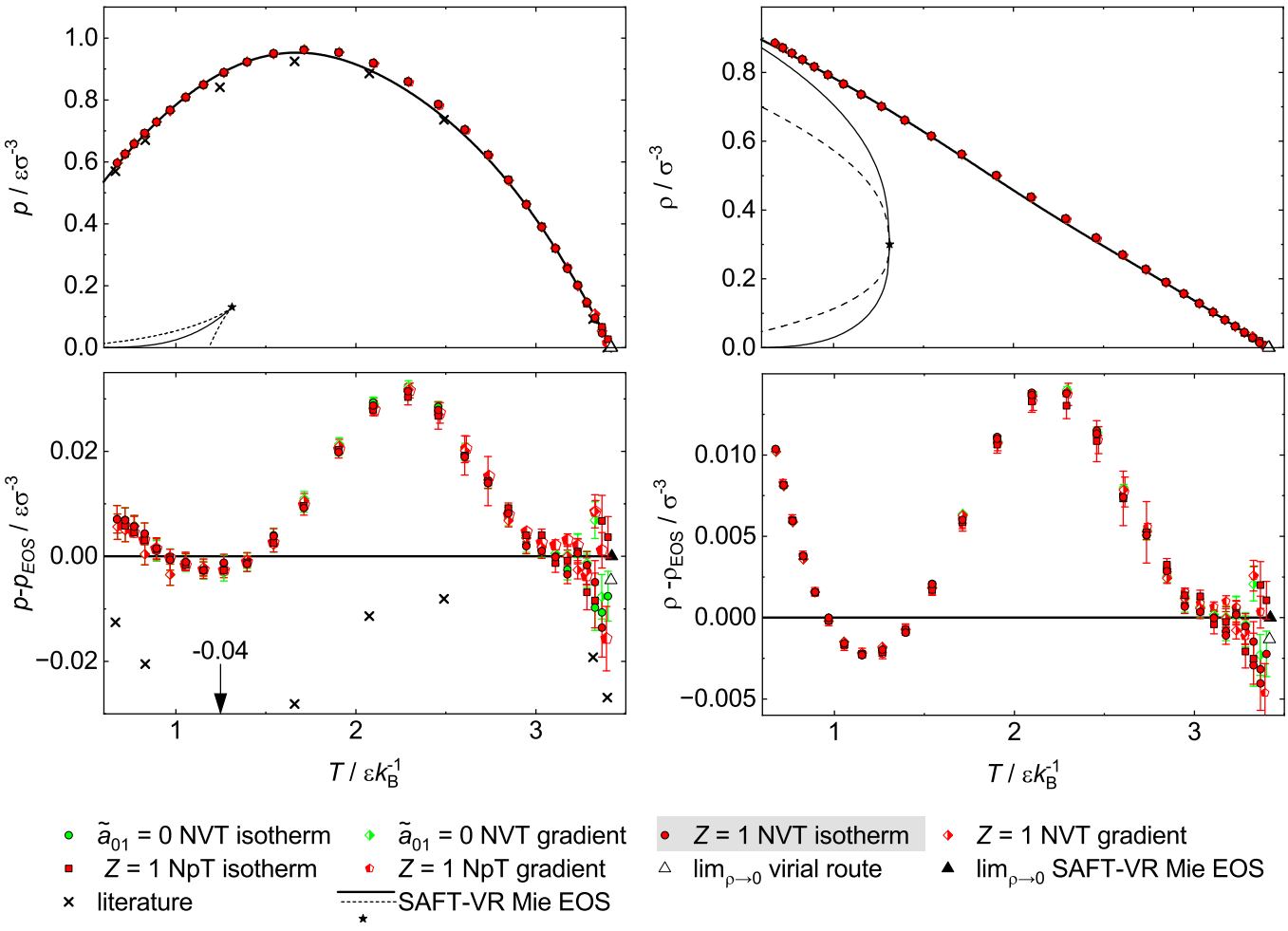

Figure 7: Results for the Zeno curve of the Lennard-Jones fluid. Left: Pressure-temperature projection; Right: density-temperature projection. Red and green symbols indicate the simulation results from this work; black crosses the results from *Deiters & Neumaier*[6] taken from the Lennard-Jones database.[14] Thick solid line and filled black triangle indicate the EOS initial guess value for the Zeno curve. The open triangle indicates the zero-density limit Zeno curve state point obtained from the virial route. The bottom row shows the deviation plots using the EOS results as a base line. Thin dashed lines, thin solid lines, and filled star indicate the EOS[36] results for the VLE binodal, spinodal, and critical point, respectively. The gray shaded area indicates the most favorable approach.

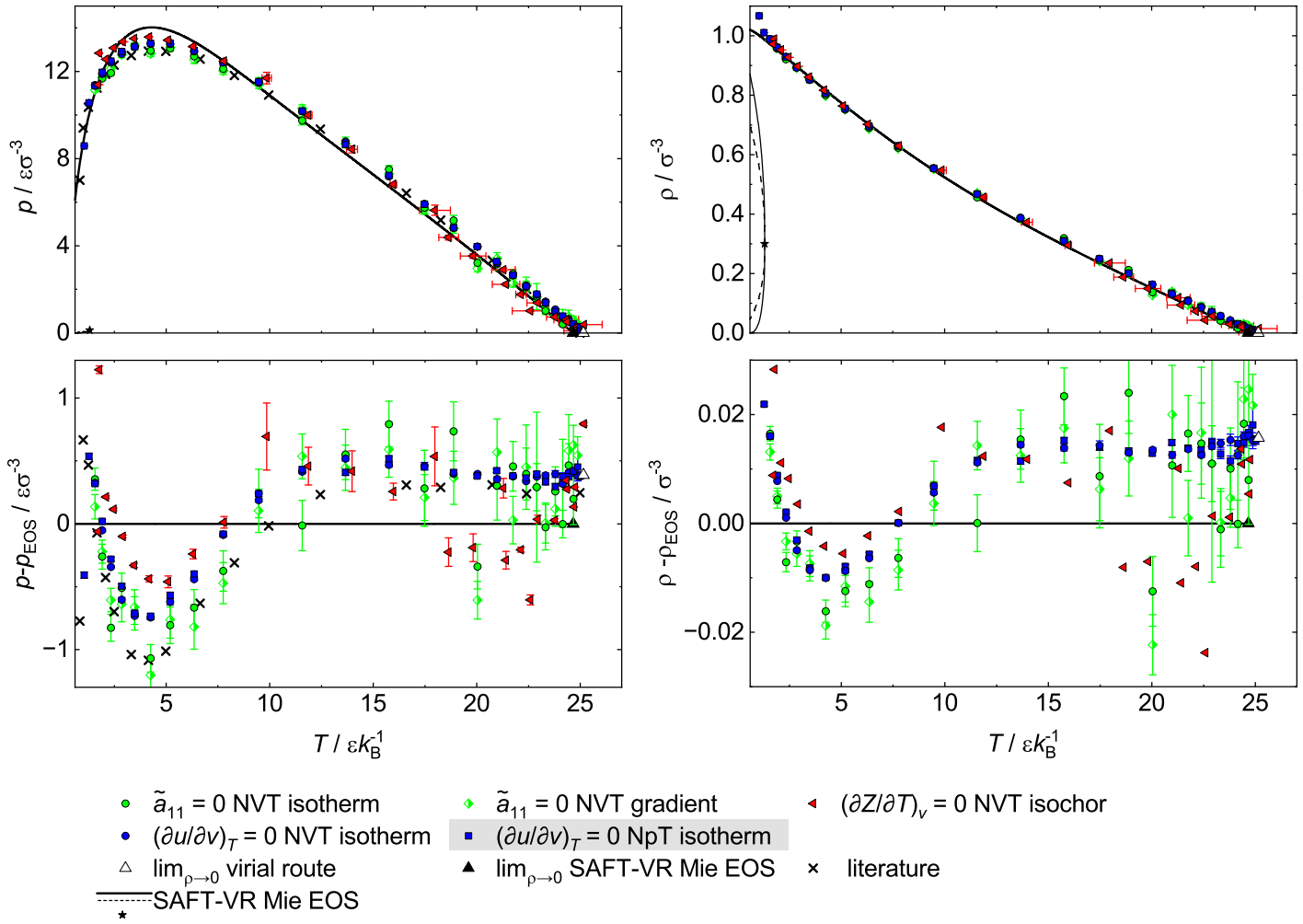

Figure 8: Results for the Amagat curve of the Lennard-Jones fluid. Left: pressure-temperature projection; Right: density-temperature projection. Red, green, and blue symbols indicate the simulation results from this work; black crosses the results from *Deiters & Neumaier*[6] taken from the Lennard-Jones database.[14] Thick solid line and filled black triangle indicate the EOS data for the Amagat curve. The open triangle indicates the zero-density limit Zeno curve state point obtained from the virial route. The bottom row shows the deviation plots using the EOS results as a base line. In the deviation plots, for data points located at higher temperatures than the zero-density limit of the EOS, a linear extrapolation of the EOS results was applied. Thin dashed lines, thin solid lines, and filled star indicate the EOS[36] results for the VLE binodal, spinodal, and critical point, respectively. The gray shaded area indicates the most favorable approach.

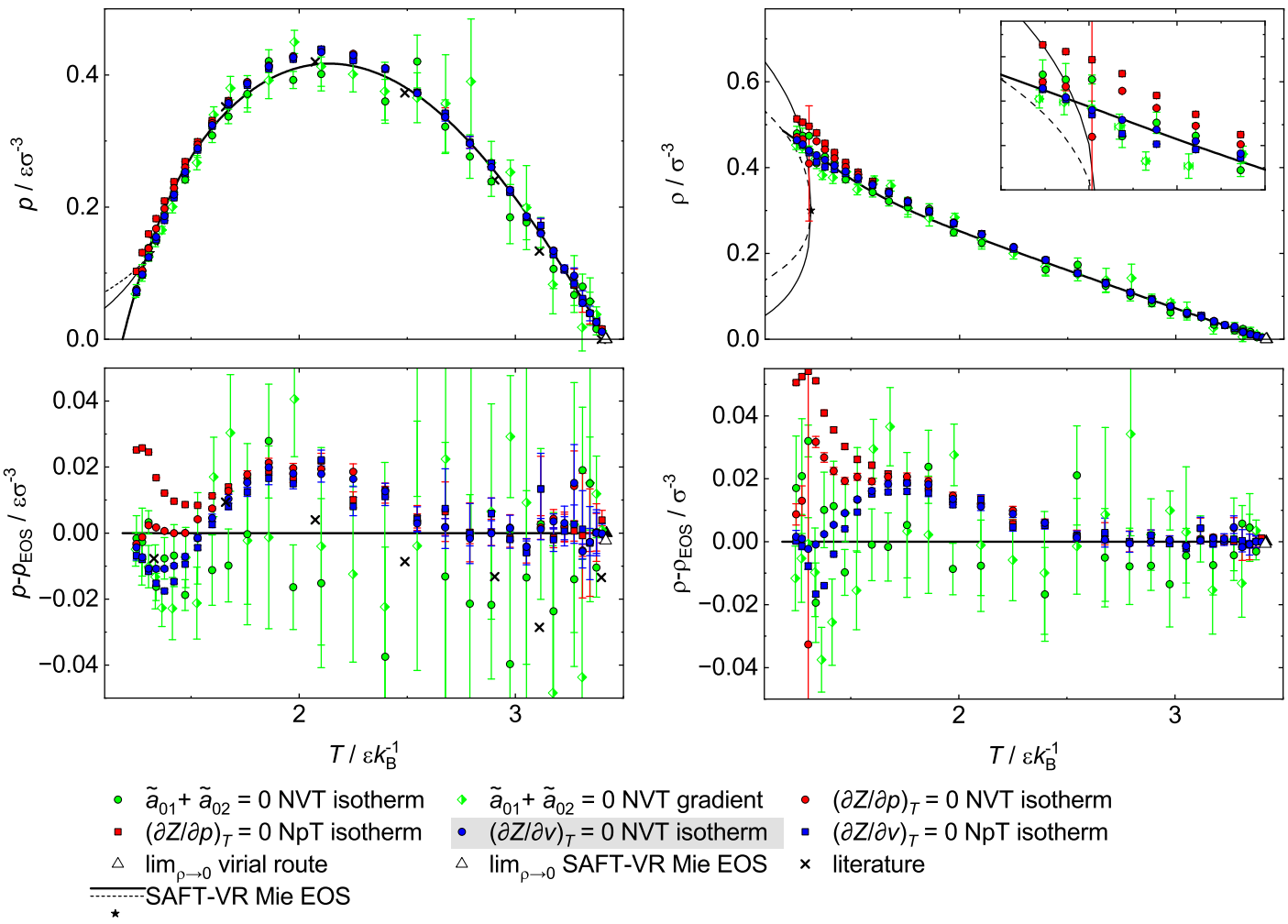

Figure 9: Results for the Boyle curve of the Lennard-Jones fluid. Left: pressure-temperature projection; Right: density-temperature projection. Red, green, and blue symbols indicate the simulation results from this work; black crosses the results from *Deiters & Neumaier*[6] taken from the Lennard-Jones database.[14] Thick solid line and filled black triangle indicate the EOS data for the Boyle curve. The open triangle indicates the zero-density limit Zeno curve state point obtained from the virial route. The bottom row shows the deviation plots using the EOS results as a base line. Thin dashed lines, thin solid lines, and filled star indicate the EOS[36] results for the VLE binodal, spinodal, and critical point, respectively. The gray shaded area indicates the most favorable approach.

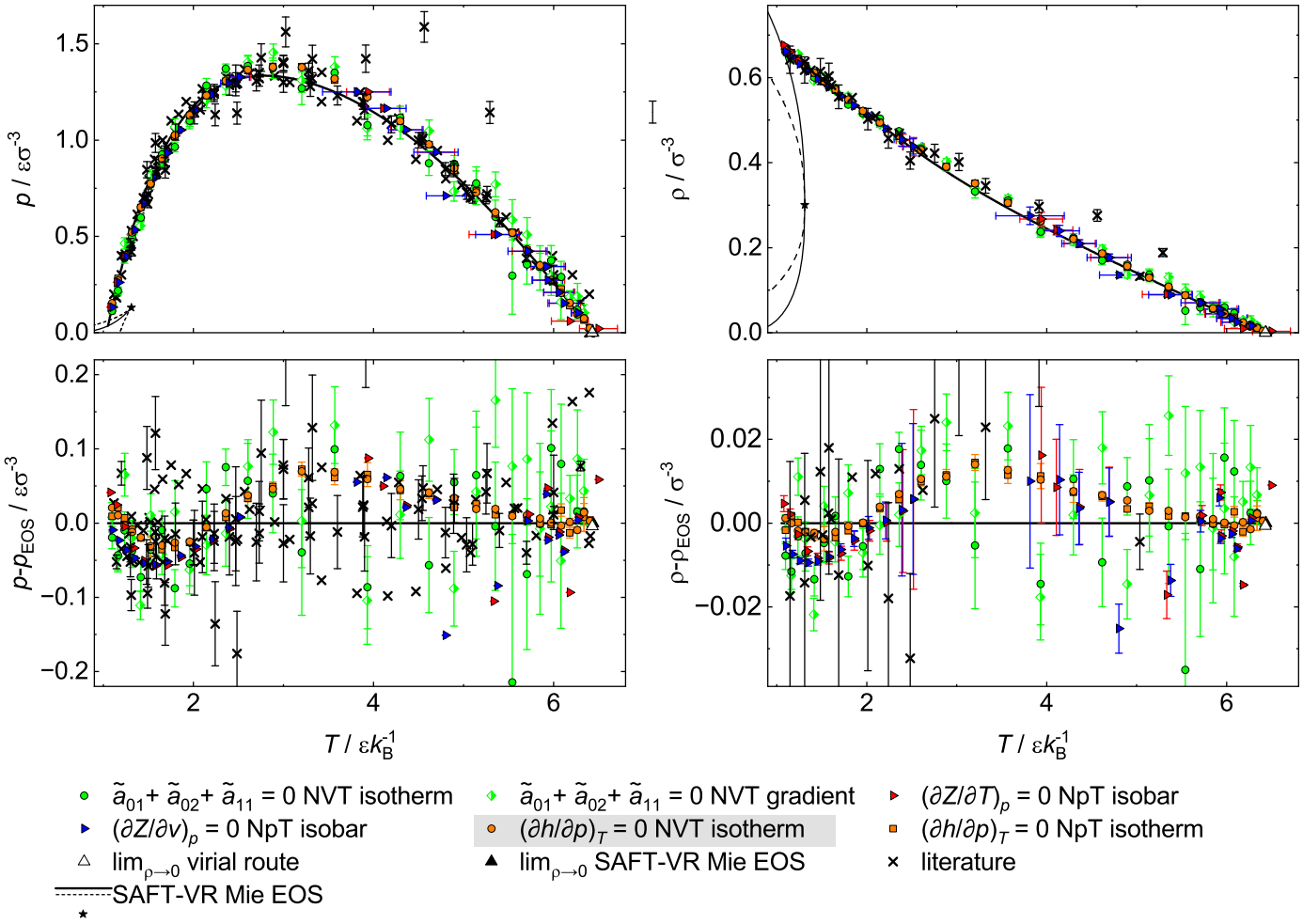

Figure 10: Results for the Charles curve of the Lennard-Jones fluid. Left: pressure-temperature projection; Right: density-temperature projection. Red, green, orange, and blue symbols indicate the simulation results from this work; black crosses results from the literature[6–8,10,48–50] taken from the Lennard-Jones database.[14] Thick solid line and filled black triangle indicate the EOS data for the Charles curve. The open triangle indicates the zero-density limit Zeno curve state point obtained from the virial route. The bottom row shows the deviation plots using the EOS results as a base line. Thin dashed lines, thin solid lines, and filled star indicate the EOS[36] results for the VLE binodal, spinodal, and critical point, respectively. The gray shaded area indicates the most favorable approach.

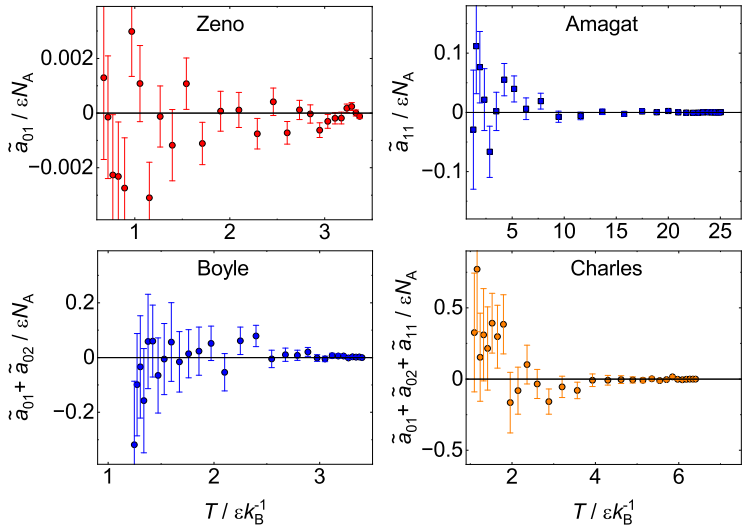

Figure 11: Consistency test for the Helmholtz energy criteria (cf. Table 1) using the Lennard-Jones fluid results from the final simulations at the determined characteristic curve state points (blue section in Fig. 2). Only results shown for the most favorable approach for each curve.

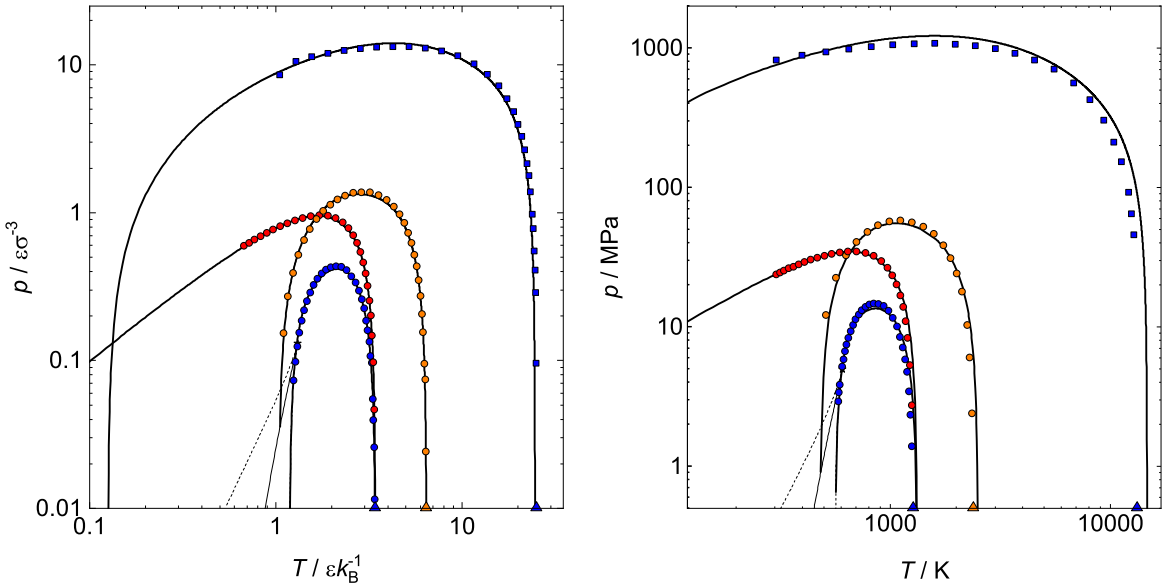

Figure 12: Characteristic curves for the Lennard-Jones fluid (left) and toluene (right) in the double logarithmic p-T projection. Only results shown for the most favorable approach for each curve. Symbols indicate the final results; thick lines the (un-corrected) EOS initial guess value. Thin dashed lines, thin solid lines, and filled star indicate the EOS results for the VLE binodal, spinodal, and critical point, respectively.

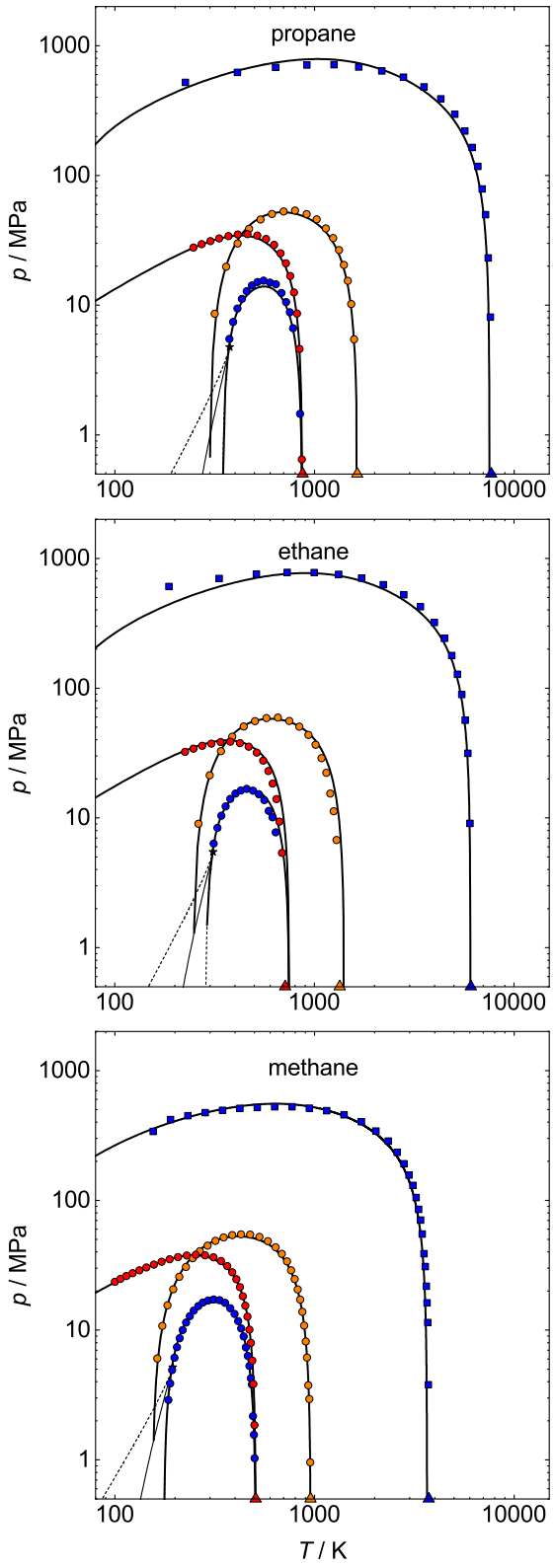

Figure 13: Characteristic curves for three alkanes in the double logarithmic p-T projection: methane (bottom), ethane (middle), and propane (top). Symbols indicate the final results; thick lines the (un-corrected) EOS initial guess value. Thin dashed lines, thin solid lines, and filled star indicate the EOS results for the VLE binodal, spinodal, and critical point, respectively.

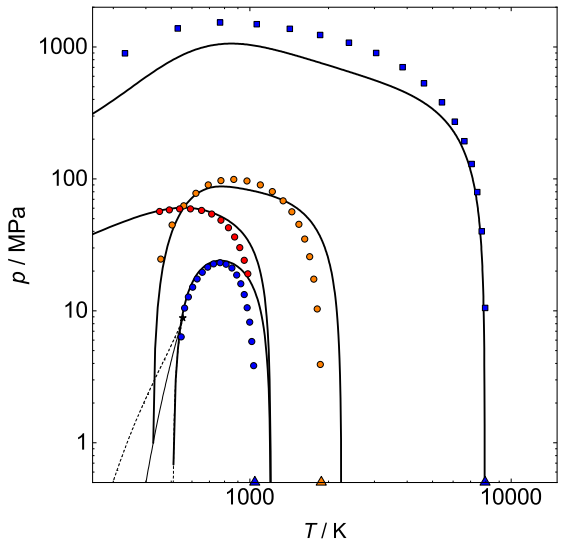

Figure 14: Characteristic curves for ethanol in the double logarithmic p-T projection. Symbols indicate the final results; thick lines the (un-corrected) EOS initial guess value. Thin dashed lines, thin solid lines, and filled star indicate the EOS results for the VLE binodal, spinodal, and critical point, respectively.

References

(1) Brown, E. H. On the thermodynamic properties of fluids. *Bulletin de lInstitut International du Froid Annexe* **1960**, *1*, 169–178.

(2) Span, R.; Wagner, W. On the extrapolation behavior of empirical equations of state. *Int. J. Thermophys.* **1997**, *18*, 1415–1443.

(3) Stephan, S.; Deiters, U. K. Characteristic Curves of the Lennard-Jones Fluid. *Int. J. Thermophys.* **2020**, *41*, 147.

(4) Alsaifi, N. M.; Elliott, J. R. Avoiding Artifacts in Noncubic Equations of State. *Ind. Eng. Chem. Res.* **2022**, *61*, 15661–15677.

(5) Deiters, U. K.; De Reuck, K. M. Guidelines for publication of equations of state-I. Pure fluids. *Chem. Eng. J.* **1998**, *69*, 69–81.

(6) Deiters, U. K.; Neumaier, A. Computer Simulation of the Characteristic Curves of Pure Fluids. *J. Chem. Eng. Data.* **2016**, *61*, 2720–2728.

(7) Vrabec, J.; Kedia, G. K.; Hasse, H. Prediction of Joule-Thomson inversion curves for pure fluids and one mixture by molecular simulation. *Cryogenics* **2005**, *45*, 253–258.

(8) Rößler, J.; Antolovic, I.; Stephan, S.; Vrabec, J. Assessment of thermodynamic models via Joule-Thomson inversion. *Fluid Phase Equilib.* **2022**, *556*, 113401.

(9) Vrabec, J.; Kumar, A.; Hasse, H. Joule-Thomson inversion curves of mixtures by molecular simulation in comparison to advanced equations of state: Natural gas as an example. *Fluid Phase Equilib.* **2007**, *258*, 34–40.

(10) Colina, C. M.; Müller, E. A. Molecular Simulation of Joule-Thomson Inversion Curves. *Int. J. Thermophys.* **1999**, *20*, 229–235.

(11) Colina, C. M.; Lisal, M.; Siperstein, F. R.; Gubbins, K. E. Accurate CO_2 Joule-Thomson inversion curve by molecular simulations. *Fluid Phase Equilib.* **2002**, *202*, 253–262.

(12) Chacin, A.; Vazquez, J.; Müller, E. Molecular simulation of the JouleThomson inversion curve of carbon dioxide. *Fluid Phase Equilib.* **1999**, *165*, 147–155.

(13) Figueroa-Gerstenmaier, S.; Lísal, M.; Nezbeda, I.; Smith, W. R.; Trejos, V. M. Prediction of isoenthalps, Joule-Thomson Coefficients and Joule-Thomson inversion curves of refrigerants by molecular simulation. *Fluid Phase Equilib.* **2014**, *375*, 143–151.

(14) Stephan, S.; Thol, M.; Vrabec, J.; Hasse, H. Thermophysical Properties of the Lennard-Jones Fluid: Database and Data Assessment. *J. Chem. Inf. Model.* **2019**, *59*, 4248–4265.

(15) Fingerhut, R.; Guevara-Carrion, G.; Nitzke, I.; Saric, D.; Marx, J.; Langenbach, K.; Prokopev, S.; Celný, D.; Bernreuther, M.; Stephan, S.; Kohns, M.; Hasse, H.; Vrabec, J. ms2: A molecular simulation tool for thermodynamic properties, release 4.0. *Comput. Phys. Commun.* **2021**, *262*, 107860.

(16) Stephan, S.; Horsch, M.; Vrabec, J.; Hasse, H. MolMod - an Open Access Database of Force Fields for Molecular Simulations of Fluids. *Mol. Simul.* **2019**, *45*, 806–814.

(17) Tchipev, N.; Seckler, S.; Heinen, M.; Vrabec, J.; Gratl, F.; Horsch, M.; Bernreuther, M.; Glass, C. W.; Niethammer, C.; Hammer, N.; Krischok, B.; Resch, M.; Kranzlmüller, D.; Hasse, H.; Bungartz, H.-J.; Neumann, P. TweTriS: Twenty trillion-atom simulation. *The International Journal of High Performance Computing Applications* **2019**, *33*, 838–854.

(18) Horsch, M.; Vrabec, J.; Hasse, H. Modification of the Classical Nucleation Theory Based on Molecular Simulation Data for Surface Tension, Critical Nucleus Size, and Nucleation Rate. *Phys. Rev. E* **2008**, *78*, 011603.

(19) Stephan, S.; Liu, J.; Langenbach, K.; Chapman, W. G.; Hasse, H. Vapor-Liquid Interface of the Lennard-Jones Truncated and Shifted Fluid: Comparison of Molecular Simulation, Density Gradient Theory, and Density Functional Theory. *J. Phys. Chem. C* **2018**, *122*, 24705–24715.

(20) Diewald, F.; Lautenschlaeger, M.; Stephan, S.; Langenbach, K.; Kuhn, C.; Seckler, S.; Bungartz, H.-J.; Hasse, H.; Müller, R. Molecular dynamics and phase field simulations of droplets on surfaces with wettability gradient. *Comput. Methods Appl. Mech. Eng.* **2020**, *361*, 112773.

(21) Vrabec, J.; Kedia, G. K.; Fuchs, G.; Hasse, H. Comprehensive study of the vapourliquid coexistence of the truncated and shifted LennardJones fluid including planar and spherical interface properties. *Mol. Phys.* **2006**, *104*, 1509–1527.

(22) Stephan, S.; Dyga, M.; Urbassek, H.; Hasse, H. The Influence of Lubrication and the Solid-Fluid Interaction on Thermodynamic Properties in a Nanoscopic Scratching Process. *Langmuir* **2019**, *35*, 16948–16960.

(23) Stephan, S.; Hasse, H. Molecular interactions at vapor-liquid interfaces: Binary mixtures of simple fluids. *Phys. Rev. E* **2020**, *101*, 012802.

(24) Deublein, S.; Eckl, B.; Stoll, J.; Lishchuk, S. V.; Guevara-Carrion, G.; Glass, C. W.; Merker, T.; Bernreuther, M.; Hasse, H.; Vrabec, J. ms2: A molecular simulation tool for thermodynamic properties. *Comput. Phys. Commun.* **2011**, *182*, 2350–2367.

(25) Rutkai, G.; Köster, A.; Guevara-Carrion, G.; Janzen, T.; Schappals, M.; Glass, C. W.; Bernreuther, M.; Wafai, A.; Stephan, S.; Kohns, M.; Reiser, S.; Deublein, S.; Horsch, M.; Hasse, H.; Vrabec, J. ms2: A molecular simulation tool for thermodynamic properties, release 3.0. *Comput. Phys. Commun.* **2017**, *221*, 343–351.

(26) Lustig, R. Statistical Thermodynamics in the Classical Molecular Dynamics Ensemble. III. Numerical Results. *J. Chem. Phys.* **1994**, *100*, 3068–3078.

(27) Lustig, R. Direct Molecular NVT Simulation of the Isobaric Heat Capacity, Speed of Sound and Joule-Thomson Coefficient. *Mol. Simul.* **2011**, *37*, 457–465.

(28) Lustig, R. Statistical analogues for fundamental equation of state derivatives. *Mol. Phys.* **2012**, *110*, 3041–3052.

(29) Guevara-Carrion, G.; Janzen, T.; Muñoz Muñoz, Y. M.; Vrabec, J. Mutual diffusion of binary liquid mixtures containing methanol, ethanol, acetone, benzene, cyclohexane, toluene, and carbon tetrachloride. *The Journal of Chemical Physics* **2016**, *144*, 124501.

(30) Vrabec, J.; Fischer, J. Vapor-liquid equilibria of binary mixtures containing methane, ethane, and carbon dioxide from molecular simulation. *International Journal of Thermophysics* **1996**, *17*, 889–908.

(31) Martin, M. G.; Siepmann, J. I. Transferable Potentials for Phase Equilibria. 1. United-Atom Description of n-Alkanes. *The Journal of Physical Chemistry B* **1998**, *102*, 2569–2577.

(32) Schnabel, T.; Vrabec, J.; Hasse, H. Henry's law constants of methane, nitrogen, oxygen and carbon dioxide in ethanol from 273 to 498 K: Prediction from molecular simulation. *Fluid Phase Equilibria* **2005**, *233*, 134–143.

(33) Vrabec, J.; Stoll, J.; Hasse, H. A Set of Molecular Models for Symmetric Quadrupolar Fluids. *The Journal of Physical Chemistry B* **2001**, *105*, 12126–12133.

(34) Heier, M.; Stephan, S.; Liu, J.; Chapman, W. G.; Hasse, H.; Langenbach, K. Equation of State for the Lennard-Jones Truncated and Shifted Fluid with a Cut-Off Radius of 2.5σ Based on Perturbation Theory and its Applications to Interfacial Thermodynamics. *Mol. Phys.* **2018**, *116*, 2083–2094.

(35) Kim, C.-H.; Vimalchand, P.; Donohue, M. D.; Sandler, S. I. Local composition model

for chainlike molecules: A new simplified version of the perturbed hard chain theory. *AIChE J.* **1986**, *32*, 1726–1734.

(36) Lafitte, T.; Apostolakou, A.; Avendano, C.; Galindo, A.; Adjiman, C. S.; Müller, E. A.; Jackson, G. Accurate Statistical Associating Fluid Theory for Chain Molecules formed from Mie Segments. *J. Chem. Phys.* **2013**, *139*, 154504.

(37) Boshkova, O. L.; Deiters, U. K. Soft Repulsion and the Behavior of Equations of State at High Pressures. *Int. J. Thermophys.* **2010**, *31*, 227–252.

(38) Chapman, W. G.; Gubbins, K. E.; Jackson, G.; Radosz, M. SAFT: Equation-of-state solution model for associating fluids. *Fluid Phase Equilib.* **1989**, *52*, 31–38.

(39) Gray, C.; Gubbins, K. *Theory of molecular fluids, Volume 1: Fundamentals*; Clarendon Press, Oxford, 1984.

(40) McQuarrie, D. A. *Statistical Mechanics*; Harper and Row: New York, 1976.

(41) Flyvbjerg, H.; Petersen, H. G. Error estimates on averages of correlated data. *J. Chem. Phys.* **1989**, *91*, 461–466.

(42) Stoll, J.; Vrabec, J.; Hasse, H.; Fischer, J. Comprehensive study of the vapour-liquid equilibria of the pure two-centre Lennard-Jones plus pointquadrupole fluid. *Fluid Phase Equilib.* **2001**, *179*, 339–362.

(43) Werth, S.; Horsch, M.; Hasse, H. Surface Tension of the Two Center Lennard-Jones Plus Quadrupole Model Fluid. *Fluid Phase Equilib.* **2015**, *392*, 12–18.

(44) Batschinski, A. Abhandlungen über Zustandsgleichung; Abh. I: Der orthometrische Zustand. *Ann. Phys.* **1906**, *324*, 307–309.

(45) Apfelbaum, E. M.; Vorob'ev, V. S.; Martynov, G. A. Virial Expansion Providing of the Linearity for a Unit Compressibility Factor. *J. Phys. Chem. A* **2004**, *108*, 10381–10385.

(46) Apfelbaum, E. M.; Vorob'ev, V. S.; Martynov, G. A. Triangle of Liquid-Gas States. *J. Phys. Chem. B* **2006**, *110*, 8474–8480.

(47) Stephan, S.; Staubach, J.; Hasse, H. Review and Comparison of Equations of State for the Lennard-Jones Fluid. *Fluid Phase Equilibr.* **2020**, *523*, 112772.

(48) Kioupis, L. I.; Arya, G.; Maginn, E. J. Pressure-Enthalpy Driven Molecular Dynamics for Thermodynamic Property Calculation II: Applications. *Fluid Phase Equilib.* **2002**, *200*, 93–110.

(49) Heyes, D. M.; Llaguno, C. T. Computer Simulation and Equation of State Study of the Boyle and Inversion Temperature of Simple Fluids. *Chem. Phys.* **1992**, *168*, 61–68.

(50) Yigzawe, T. M.; Sadus, R. J. Intermolecular Interactions and the Thermodynamic Properties of Supercritical Fluids. *J. Chem. Phys.* **2013**, *138*, 194502.

TOC Graphic

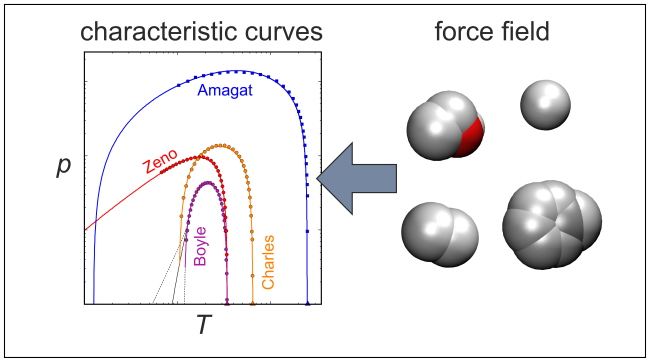
characteristic curves
force field
Amagat
Zeno
Boyle
Charles
p
T